Monthly Notices of the ROYAL ASTRONOMICAL SOCIETY

MNRAS **526,** 3540–3547 (2023) https://doi.org/10.1093/mnras/stad2801
Advance Access publication 2023 September 14

A remarkably stable accretion disc in the Seyfert galaxy MCG-5-23-16

Roberto Serafinelli [1]★ Andrea Marinucci [2] Alessandra De Rosa [1] Stefano Bianchi [3] Riccardo Middei [4,5] Giorgio Matt,[3] James N. Reeves,[6,7] Valentina Braito [7,6,8] Francesco Tombesi,[9,5,10,11,12] Vittoria E. Gianolli [3,13] Adam Ingram [14] Frédéric Marin [15] Pierre-Olivier Petrucci,[13] Daniele Tagliacozzo [3] and Francesco Ursini [3]

[1]*INAF – Istituto di Astrofisica e Planetologia Spaziali, Via del Fosso del Cavaliere 100, I-00133 Roma, Italy*
[2]*ASI – Agenzia Spaziale Italiana, Via del Politecnico snc, I-000133 Roma, Italy*
[3]*Dipartimento di Matematica e Fisica, Università degli Studi Roma Tre, Via della Vasca Navale 84, I-00146 Roma, Italy*
[4]*Space Science Data Center, Agenzia Spaziale Italiana, Via del Politecnico snc, I-00133 Roma, Italy*
[5]*INAF – Osservatorio Astronomico di Roma, Via Frascati 33, Monte Porzio Catone, I-00078 Roma, Italy*
[6]*Department of Physics, Institute for Astrophysics and Computational Sciences, The Catholic University of America, Washington, DC 20064, USA*
[7]*INAF – Osservatorio Astronomico di Brera, Via Bianchi 46, I-23807 Merate (LC), Italy*
[8]*Dipartimento di Fisica, Università di Trento, Via Sommarive 14, I-38123 Trento, Italy*
[9]*Dipartimento di Fisica, Università degli Studi di Roma Tor Vergata, Via della Ricerca Scientifica 1, I-00133 Roma, Italy*
[10]*INFN – Istituto Nazionale di Fisica Nucleare, Sezione di Roma 'Tor Vergata', Via della Ricerca Scientifica 1, I-00133 Roma, Italy*
[11]*Department of Astronomy, University of Maryland, College Park, MD 20742, USA*
[12]*NASA Goddard Space Flight Center, Code 662, Greenbelt, MD 20771, USA*
[13]*CNRS, IPAG, Université Grenoble Alpes, F-38000 Grenoble, France*
[14]*School of Mathematics, Statistics, and Physics, Newcastle University, Newcastle Upon Tyne NE1 7RU, UK*
[15]*CNRS, Observatoire Astrononomique de Strasbourg, Université de Strasbourg, UMR 7550, F-67000 Strasbourg, France*

Accepted 2023 September 7. Received 2023 August 11; in original form 2023 May 29

ABSTRACT

MCG-5-23-16 is a Seyfert 1.9 galaxy at redshift $z = 0.008\,49$. We analyse here the X-ray spectra obtained with *X-ray Multi-Mirror (XMM)-Newton* and *Nuclear Spectroscopic Telescope Array* (*NuSTAR*) data, which are the first contemporaneous observations with these two X-ray telescopes. Two reflection features, producing a narrow core and a broad component of the Fe Kα, are clearly detected in the data. The analysis of the broad iron line shows evidence of a truncated disc with inner radius $R_{\rm in} = 40^{+23}_{-16}$ R_g and an inclination of $41^{+9}_{-10}{}^{\circ}$. The high quality of the *NuSTAR* observations allows us to measure a high-energy cut-off at $E_{\rm cut} = 131^{+10}_{-9}$ keV. We also analyse the reflection grating spectrometer spectrum, finding that the soft X-ray emission is produced by two photoionized plasma emission regions, with different ionization parameters and similar column densities. Remarkably, the source only shows moderate continuum flux variability, keeping the spectral shape roughly constant in a time-scale of ∼20 yr.

Key words: galaxies: active – galaxies: individual: MCG-5-23-16 – X-rays: galaxies.

1 INTRODUCTION

The X-ray emission of active galactic nuclei (AGNs) is thought to be produced by Comptonization of ultraviolet (UV) seed photons coming from an accretion disc around a supermassive black hole (SMBH), by a hot corona, located in the innermost region around the SMBH (e.g. Haardt & Maraschi 1991, 1993). The X-ray spectrum of an AGN typically assumes the shape of a power law, characterized by a photon index Γ, up to a characteristic cut-off energy $E_{\rm cut}$, where the power law breaks. Both Γ and $E_{\rm cut}$ are related to the physical properties of the corona, such as the electron temperature $kT_{\rm e}$ and the optical depth $\tau_{\rm e}$ (e.g. Shapiro, Lightman & Eardley 1976; Sunyaev & Titarchuk 1980; Lightman & Zdziarski 1987; Petrucci et al. 2001; Middei et al. 2019). However, these relations are strongly dependent on the geometry of the corona, which is still largely unknown.

Several measurements of the cut-off energy and/or the coronal temperature have been obtained with high-energy instruments such as *Beppo-SAX* (e.g. Dadina 2007), *INTEGRAL* (De Rosa et al. 2012), and *Swift*-BAT (e.g. Ricci et al. 2017), but the launch of Nuclear Spectroscopic Telescope Array (*NuSTAR*) in 2013, with its unprecedented sensitivity in the $E > 10$ keV energy band has revolutionized the field, providing high-precision cut-off energy measurements for dozens of AGNs (e.g. Fabian et al. 2015, 2017). The availability of high-quality measurements of the cut-off energy or coronal temperature, even for absorbed sources (e.g. Baloković et al. 2020; Middei et al. 2021; Serafinelli et al. 2023), allowed several authors to study the relation between the cut-off energy and physical parameters of the AGNs, finding that it is not dependent on the black hole mass $M_{\rm BH}$ or the accretion rate $L/L_{\rm Edd}$ (e.g. Tortosa et al. 2018; Kamraj et al. 2022, Serafinelli et al., in preparation).

However, the values of $kT_{\rm e}$ and $\tau_{\rm e}$ are degenerate with the cut-off energy and photon index, as spectroscopy alone is not able to distinguish between different geometries (e.g. Middei et al. 2019;

★ E-mail: roberto.serafinelli@inaf.it

© 2023 The Author(s)
Published by Oxford University Press on behalf of Royal Astronomical Society

Downloaded from https://academic.oup.com/mnras/article/526/3/3540/7274144 by guest on 04 December 2024

Ursini et al. 2022), such as slab-like (e.g. Haardt & Maraschi 1991), spherical (e.g. Frontera et al. 2003), and lamp-post (e.g. Miniutti & Fabian 2004). Recently, the first coronal X-ray polarization measurement has been obtained with the *Imaging X-ray Polarization Explorer* (*IXPE*) in the Seyfert galaxy NGC 4151 (Gianolli et al. 2023). The favoured geometry for the hot corona is a slab or a wedge distributed over the accretion disc (see Poutanen, Veledina & Zdziarski 2018, for a description of the latter).

MCG-5-23-16 is a Seyfert 1.9 galaxy (Véron et al. 1980) at redshift $z = 0.008\,49$. Due to its high X-ray flux ($F_{2-10\,\mathrm{keV}} \simeq 8 \times 10^{-11}$ erg cm^{-2} s^{-1}), the object was observed several times by many X-ray facilities in the last few decades.

The X-ray spectrum of this AGN is characterized by moderate neutral absorption ($N_{\mathrm{H}} \simeq 1.3 \times 10^{22}$ cm^{-2}) and by the presence of a soft excess and complex Fe Kα emission. Evidence of a broad Fe Kα line on this source was found with *Advanced Satellite for Cosmology and Astrophysics* (ASCA, Weaver et al. 1997) and later confirmed by *X-ray Multi-Mirror* (*XMM*)*–Newton* observations (Dewangan, Griffiths & Schurch 2003; Balestra, Bianchi & Matt 2004), pointing to the presence of two reflectors, one responsible for a narrow core at 6.4 keV and one responsible for the broad wing, likely originated very close to the black hole.

The broad line was explored with *Suzaku* (Reeves et al. 2007), and it was found that it is originated from a disc with inner radius of $\sim 40R_g$, where $R_g = GM/c^2$ is the gravitational radius, from the central black hole, and inclination of $\sim 50^\circ$. Braito et al. (2007) analysed a long simultaneous *XMM–Newton* (131 ks) and *Chandra* (50 ks) observation, which was able to confirm these results on the broad Fe Kα line. Additionally, these data unveiled the presence of an absorption feature at 7.7 keV, hinting at the possible presence of ionized iron outflowing at $\sim 0.1c$, i.e. an ultrafast outflow (UFO; e.g. Pounds et al. 2003; Tombesi et al. 2010; Serafinelli et al. 2019; Matzeu et al. 2023). Moreover, the reflection grating spectrometer (RGS) data allowed the detection of emission lines from ionized gas, pointing to a narrow-line region origin of the soft excess.

The source was also observed by *NuSTAR*, which allowed the first accurate measurement of the cut-off energy ($E \simeq 120$ keV; Baloković et al. 2015), and also hinting at its possible variability (Zoghbi et al. 2017). At the same time, *NuSTAR* confirmed the line parameters, such as the disc inner radius and inclination.

Finally, MCG-5-23-16 was targeted by two pointings in 2022 with *IXPE* of 486 ks (Marinucci et al. 2022) and 642 ks (Tagliacozzo et al. 2023), respectively. The combined observations yielded an upper limit $\Pi_{\mathrm{max}} = 3.2$ on the polarization degree, in the 2–8 keV energy band.

Here, we present the analysis of the *XMM–Newton* and *NuSTAR* observations, the latter being taken together with the two *IXPE* pointings. In Section 2, we report on the data and the data reduction techniques that we adopted. We describe the spectral analysis, first performed in the 3–79 keV band and then expanded to the broad band ($E = 0.3$–79 keV) in Section 3. We summarize the results in Section 5. Throughout the paper, we adopt a standard flat Lambda cold dark matter cosmology with $H_0 = 70$ km s^{-1} Mpc^{-1}, $\Omega_{\mathrm{m}} = 0.3$, and $\Omega_\Lambda = 0.7$.

2 DATA REDUCTION

The data analysed here consists of contemporaneous *XMM–Newton* (OBSID 0890670101, 92 ks elapsed exposure time, 56 ks net) and *NuSTAR* observation (OBSID 60701014002, 83 ks), complementary to the *IXPE* observations analysed in Marinucci et al. (2022), taken in 2022 May (Epoch 1). Additionally, the data set includes a further *NuSTAR* pointing (OBSID 90801630002, 85 ks), contemporaneous with the *IXPE* observation reported in Tagliacozzo et al. (2023), taken in 2022 November (Epoch 2). The data are summarized in Table 1.

Table 1. The data used in this paper. One of the *NuSTAR* observations is contemporaneous with *XMM–Newton* at Epoch 1. The *XMM–Newton* exposure is only the one from EPIC-pn, while the *NuSTAR* exposure must be read as per FPM detector.

Epoch	Instrument	OBSID	Date	Exposure (s)
1	*XMM–Newton*	0890 670 101	2022-05-21	92 700
1	*NuSTAR*	60 701 014 002	2022-05-21	83 676
2	*NuSTAR*	90 801 630 002	2022-11-11	85 743

We extract the event list from the EPIC-pn camera using the standard System Analysis Software (SAS) version 20.0.0 tool EPPROC, and we remove the flaring events (e.g. De Luca & Molendi 2004) adopting an appropriate filtering to veto all those times where the observation is affected by flaring. We also extract the MOS spectra using the tool EMPROC, but they are severely affected by pile-up (e.g. Ballet 1999) and therefore they are not analysed here. The EPIC-pn spectrum is extracted by selecting a 40 arcsec radius region on the source, while the background is extracted on a source-free region of the same size. The response matrix and ancillary files are extracted with the standard tools RMFGEN and ARFGEN, respectively. We corrected the effective area with APPLYABSFLUXCORR, for a better agreement with *NuSTAR* data. The spectrum is grouped at a minimum of 100 counts per energy bin. We consider the energy range $E = 0.5$–10 keV for the EPIC-pn spectrum. We also reduce the RGS1 and RGS2 spectra using the RGSPROC task in SAS, with response matrices produced with RGSRMFGEN. We combine the two RGS spectra using RGSCOMBINE and we consider the energy band $E = 0.5$–2 keV, i.e. $\lambda = 6$–25 Å.

The *NuSTAR* data are reduced by using the HEASOFT v6.30 task NUPIPELINE, from the NUSTARDAS software package. We used CALDB calibration files updated as of 2022 August 29. For each observation, we extract spectra from the two Focal Plane Modules A and B (FPMA and FPMB) by selecting a region with 60 arcsec radius around the source, and two source-free regions with 40 arcsec radius for the background. Both the detectors FPMA and FPMB are grouped at a minimum of 100 counts per energy bin, for each observation. We consider the energy band $E = 3$–79 keV for these data sets.

3 SPECTRAL ANALYSIS

We use the software XSPEC v12.12.0 (Arnaud 1996) to perform all spectral fits in this paper. The errors are reported at 90 per cent confidence level, corresponding to $\Delta\chi^2 = 2.71$. All models include a cross-calibration constant between the FPM modules and EPIC-pn, and in all our models is well fitted by the value $C_{\mathrm{FPMA/pn}} = 1.39 \pm 0.01$ and $C_{\mathrm{FPMB/pn}} = 1.42 \pm 0.01$. We assumed that these constants do not change between the two *NuSTAR* observations, while we let the normalizations free to take into account flux differences. For each epoch, the two FPM modules are fitted separately, but keeping each parameter of the fit tied together with the exception of the calibration constant. Following recent works (e.g. Gianolli et al. 2023; Ingram et al. 2023), we shift models that include lines with fixed centroid energies using the XSPEC model VASHIFT, to counter the possible presence of calibration issues. We leave the velocity free in the EPIC-pn data, and in the two FPMA spectra, with the shift velocities in the two FPMB observations tied to the simultaneous FPMA. In all models, we find a shift of $v_{\mathrm{shift},XMM} = 2200 \pm 300$ km

Downloaded from https://academic.oup.com/mnras/article/526/3/3540/7274144 by guest on 04 December 2024

s^{-1} and $v_{\mathrm{shift},NuSTAR,1} = 4300 \pm 900$ km s^{-1} and $v_{\mathrm{shift},\,NuSTAR,2} = 5500 \pm 1000$ km s^{-1} for EPIC-pn and the FPM modules in Epochs 1 and 2, respectively. Initially, we assume that the spectral shape does not change between Epochs 1 and 2, therefore we keep Γ and E_{cut} tied. The possible variability of these two parameters is discussed in Section 4.1.

3.1 Hard band spectral analysis

As a first step, we only consider the spectral region between 3 and 10 keV for EPIC-pn and both observations of the FPMA and FPMB modules. In order to characterize the shape of the X-ray continuum we also exclude the 5–7.5 keV region where the iron line is predominant. In all models, we fit the continuum with a simple cut-off power law, absorbed by both Galactic ($N_{\mathrm{H,Gal}} = 8 \times 10^{20}$ cm^{-2}, HI4PI Collaboration 2016) and systemic absorption, using TBABS and ZTBABS, respectively. We find a photon index $\Gamma = 1.86 \pm 0.01$ and an absorption column density $N_{\mathrm{H}} = (1.6 \pm 0.1) \times 10^{22}$ cm^{-2}, with an acceptable goodness of fit, χ^2/dof = 604/540, where dof is the degree of freedom. However, when extrapolated to the energy bands $E < 3$ and $E > 10$ keV, significant residuals arise, due to the presence of a soft X-ray emission and a reflection component, respectively (see upper panel in Fig. 1). Moreover, the residuals in the 5–9 keV energy band show a complex emission including narrow Fe Kα and Kβ emission lines, and the presence of a broad component of the Fe Kα emission line (see lower panel of Fig. 1). At first, we decide to only fit the 3–79 keV energy band of the spectrum, ignoring the EPIC-pn spectrum below 3 keV. This choice allows us to find disc parameters with simpler models, not affected by the presence of soft X-ray emission, which then will be used as a starting point for the broad-band fits.

Our first attempt at fitting the 3–79 keV energy band is made by considering a cut-off power law at redshift $z = 0.008\,49$ (ZCUTOFFPL), and two Fe emission lines. The first emission line represents the typical Fe Kα fluorescent line. We find the centroid energy of the Kα line at $E = 6.36^{+0.02}_{-0.01}$ keV, which is clear evidence of the presence of the calibration issue mentioned in the previous section, as the rest-frame Fe Kα line is typically found at 6.4 keV. The intrinsic width of the narrow Kα line was resolved in the *Chandra* HETG observation (Braito et al. 2007) to be about 30 eV, which is therefore adopted as a fixed value for our model. We also include a narrow Fe Kβ emission line, with fixed centroid energy $E_{\mathrm{K}\beta} = 7.06$ keV and intrinsic width 30 eV. The normalization of the Kβ emission line is assumed to be 13 per cent of that of the Kα line (e.g. Palmeri et al. 2003). The fit statistics is χ^2/dof = 3185/2152.

As highlighted by previous observations (e.g. Weaver et al. 1997; Braito et al. 2007; Reeves et al. 2007; Baloković et al. 2015; Zoghbi et al. 2017), this source typically shows a well-defined broad iron line in addition to the narrow ones, therefore we add a second Fe Kα emission line, this time keeping the width free. We find a line centred at $E = 6.19^{+0.05}_{-0.06}$ keV with a width of $\sigma = 270^{+60}_{-70}$ eV. The statistic improves to χ^2/dof = 2919/2149. We note that the blue wing of the broad Fe Kα line is degenerate with the possible presence of ionized Fe XXV and Fe XXVI because of the insufficient spectral resolution.

Finally, we also add a reflection component, modelled with PEXRAV (Magdziarz & Zdziarski 1995), as pure reflection, i.e. we fix $\mathcal{R} = -1$, with its normalization allowed to vary independently from the same-epoch power law. We note that all reflection models in this paper are assumed as pure reflection components. Moreover, the continuum parameters of the reflectors (Γ and E_{cut}) are tied to the ones of the primary continuum. We leave the normalization of PEXRAV in

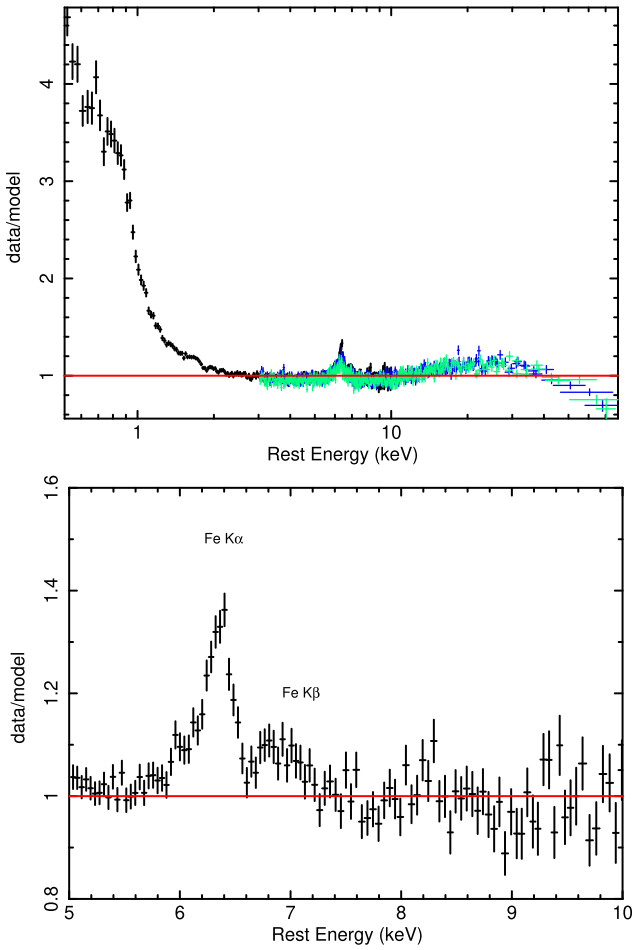


Figure 1. *Upper*: Broad-band (0.3–79 keV) residuals when the main continuum is fitted in the 3–5 and 7.5–10 spectral regions. The black spectrum represents the EPIC-pn data, FPMA and FPMB data are shown in the same colour, blue for Epoch 1 and green for Epoch 2. *Lower*: Zoom on the 5–10 keV spectral region, with *XMM–Newton* (EPIC-pn, black) as a ratio to an absorbed power law with a photon index $\Gamma = 1.86$ and a column density $N_{\mathrm{H}} = 1.6 \times 10^{22}$ cm^{-2}.

Epochs 1 and 2 to vary independently. We assume solar abundances, including iron, and assume the default value $\cos\iota = 0.45$ for the inclination. The final statistic for this model, which we denote as Model A, is χ^2/dof = 2343/2147 = 1.09 (see Table 2).

The iron K emission line complex is best fitted by a narrow and a broad component with width $\sigma_{\mathrm{K}\alpha,\mathrm{b}} = 270 \pm 70$ eV. The latter is most likely produced by reprocessed radiation on the accretion disc, therefore we replace the broad Gaussian line with the accretion disc line emission RELLINE (Dauser et al. 2010). Given that the iron line is not extremely broad like other Seyfert galaxies such as MCG-6-30-15 (e.g. Marinucci et al. 2014), we initially adopt a disc radial emissivity index $\beta = -3$ up to $R = 1000\,R_g$, an inclination of 45° (Reeves et al. 2007) and a non-spinning black hole $a = 0$. We also tie the centroid energy to the one of the narrow Fe Kα emission line. The result of this fit shows evidence of a truncated disc with inner radius $R_{\mathrm{in}} > 36\,R_g$, which is consistent with previous results on this source (e.g. Reeves et al. 2007). The statistic for this model is χ^2/dof = 2368/2148. If we assume a maximally spinning black hole ($a = 0.998$), the result is unchanged. Indeed, as the disc is truncated, we are not able to infer the Innermost Stable Circular Orbit (ISCO) from the emission line profile and, in turn, the fit does not allow us to

Downloaded from https://academic.oup.com/mnras/article/526/3/3540/7274144 by guest on 04 December 2024

Table 2. Table of the various models used for the hard X-ray spectrum ($E =$ 3–79 keV). $*$ Frozen parameters.

Parameter	Model A	Model B
Absorption		
$N_{\rm H}$ (10^{22} cm^{-2})	1.5 ± 0.1	1.7 ± 0.2
Continuum		
Γ	1.88 ± 0.02	1.93 ± 0.04
E_c (keV)	135^{+18}_{-14}	180^{+50}_{-30}
Norm$_{\rm PL,obs1}$ (10^{-2} cm^{-2} s^{-1} keV^{-1})	2.7 ± 0.1	2.8 ± 0.2
Norm$_{\rm PL,obs2}$ (10^{-2} cm^{-2} s^{-1} keV^{-1})	2.8 ± 0.1	3.0 ± 0.2
Slab reflection (PEXRAV)		
Abundance	1*	–
Fe abundance	1*	–
Cos ι	0.45*	–
Norm$_{\rm PEX,obs1}$ (10^{-2} cm^{-2} s^{-1} keV^{-1})	$2.2^{+0.3}_{-0.2}$	–
Norm$_{\rm PEX,obs2}$ (10^{-2} cm^{-2} s^{-1} keV^{-1})	2.3 ± 0.3	–
Narrow emission lines		
$E_{{\rm K}\alpha,{\rm n}}$ (keV)	$6.36^{+0.02}_{-0.01}$	–
EW$_{{\rm K}\alpha,{\rm n}}$ (eV)	49^{+7}_{-9}	–
σ	0*	–
Norm$_{{\rm K}\alpha,{\rm n}}$ (10^{-5} cm^{-2} s^{-1} keV^{-1})	$4.6^{+0.7}_{-0.8}$	–
$E_{{\rm K}\beta,{\rm n}}$ (keV)	7.06*	–
EW$_{{\rm K}\beta,{\rm n}}$ (eV)	10 ± 2	–
Broad iron line		
$E_{{\rm K}\alpha,{\rm b}}$ (keV)	$6.19^{+0.05}_{-0.06}$	–
$\sigma_{{\rm K}\alpha,{\rm b}}$ (keV)	$0.27^{+0.06}_{-0.07}$	–
EW$_{{\rm K}\alpha,{\rm b}}$ (eV)	56^{+9}_{-11}	–
norm$_{{\rm K}\alpha,{\rm b}}$ (10^{-5} cm^{-2} s^{-1} keV^{-1})	5 ± 1	–
Distant reflection (XILLVER)		
Fe abundance	–	$0.9^{+0.2}_{-0.1}$
Inclination ($^\circ$)	–	45$^{\circ *}$
log ξ (erg cm s^{-1})	–	0*
Norm$_{\rm XIL,obs1}$ (10^{-4} cm^{-2} s^{-1} keV^{-1})	–	$2.6^{+0.4}_{-0.2}$
Norm$_{\rm XIL,obs2}$ (10^{-4} cm^{-2} s^{-1} keV^{-1})	–	$3.0^{+0.5}_{-0.4}$
Relativistic disc reflection (RELXILL)		
$R_{\rm in}$ (R_g)	–	56^{+32}_{-19}
a	–	0*
Log ξ	–	2.7 ± 0.1
Inclination ($^\circ$)	–	45*
Norm$_{\rm REL,obs1}$ (10^{-5} cm^{-2} s^{-1} keV^{-1})	–	7 ± 2
Norm$_{\rm REL,obs2}$ (10^{-5} cm^{-2} s^{-1} keV^{-1})	–	3^{+3}_{-2}
Velocity shift (VASHIFT)		
$v_{\rm shift}$ (km s^{-1}) *XMM–Newton*	–	2200 ± 300
$v_{\rm shift}$ (km s^{-1}) *NuSTAR* (Epoch 1)	–	4300 ± 900
$v_{\rm shift}$ (km s^{-1}) *NuSTAR* (Epoch 2)	–	5500 ± 1000
$C_{\rm FPMA/pn}$	1.39 ± 0.01	1.39 ± 0.01
$C_{\rm FPMB/pn}$	1.42 ± 0.01	1.42 ± 0.01
χ^2/dof	2343/2147	2314/2149

measure the black hole spin. Therefore, we will assume $a = 0$ in all models in this paper. We also test a different disc radial emissivity profile, assuming a broken power-law model with β fixed to -3 in the outer regions ($R > 30\ R_g$), while it is left free to vary between $R_{\rm in} = 6\ R_g$ and $30\ R_g$. This fit provides $\beta < 0$ in the inner regions ($R < 30\ R_g$), which is still consistent with a truncated disc scenario, indicating a poor contribution of the disc to the line emission for $R < 30\ R_g$. We will therefore assume an emissivity index of -3 over the whole accretion disc from here on, as it is a typical value for accretion discs above $\sim 30\, R_g$ (Wilkins & Fabian 2012).

However, iron lines likely arise from reflection processes. The presence of both a narrow and a broad iron emission line strongly suggest the presence of two reflection components, a distant one

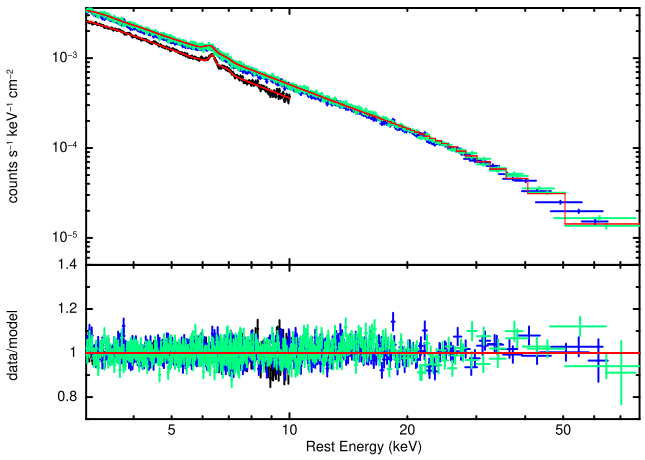


Figure 2. *Top:* the 3–79 keV spectrum analysed here. The black spectrum is the EPIC-pn from *XMM–Newton*, while blue and green spectra are the *NuSTAR* observations of Epochs 1 and 2, respectively. The two FPM spectra of each observation have been plotted with the same colour and rebinned for visual purposes only. *Bottom*: data-to-model ratio of EPIC-pn and FPM spectra in the 3–79 keV band, when modelled with Model B.

describing the narrow core and a second one representing the reflection on material much closer to the black hole, i.e. the accretion disc. Therefore, we replace the Gaussian and the relativistic lines and the PEXRAV reflection model with two reflection continua that also take into account emission lines. For the distant reflector (including the narrow Fe Kα line) we use the ionized slab reflector model XILLVER (García & Kallman 2010; García et al. 2013), that takes into account the most recent atomic data for the iron K fluorescent lines. We fix the value of the inclination to 45°, and we fit the iron abundance, the ionization and the normalization of the slab reflector. We find an upper limit for the ionization parameter log ξ/(erg cm s^{-1}) < 1.3, which is in agreement with a narrow Fe K fluorescent complex emitted from a distant reflector, for which a poorly ionized medium is expected. The iron abundance is best fitted by $A_{\rm Fe} = 0.9^{+0.2}_{-0.1}$.

Finally, we interpret the broad iron line as the product of a reflection component from the inner accretion disc, and we model this emission with the relativistic reflection model RELXILL (Dauser et al. 2014; García et al. 2014). This model is able to estimate the inner radius of the accretion disc $R_{\rm in}$, the radial emissivity index, and the spin of the black hole a, in addition to every parameter also measured by XILLVER. However, since these three parameters are degenerate, we assume an emissivity index of -3, as discussed above. We assume a non-spinning black hole with frozen spin $a = 0$. The inner radius of the accretion disc is found to be $R_{\rm in} = 56^{+32}_{-19}\ R_g$. We stress that also with this model, choosing different values of the black hole spin does not change any of the other parameters, nor the goodness of fit. This is expected, because, as already anticipated, the region producing the broad iron line does not extend to the ISCO, therefore impeding the measurement of the black hole spin. The inclination of the accretion disc is assumed to be aligned with the inclination of the most distant reflector, hence also fixed at $\iota = 45°$. We also assume that the iron abundance is the same between the two reflectors. The best-fitting ionization of the accretion disc is log ξ/(erg cm s^{-1}) $= 2.7 \pm 0.1$.

The final statistic for this model (Model B) is χ^2/dof $= 2314/2149 = 1.07$. The hard band X-ray spectrum and data-to-model ratios relative to Model B are shown in Fig. 2. A summary of the best-fitting values obtained in the hard band is listed in Table 2.

Downloaded from https://academic.oup.com/mnras/article/526/3/3540/7274144 by guest on 04 December 2024

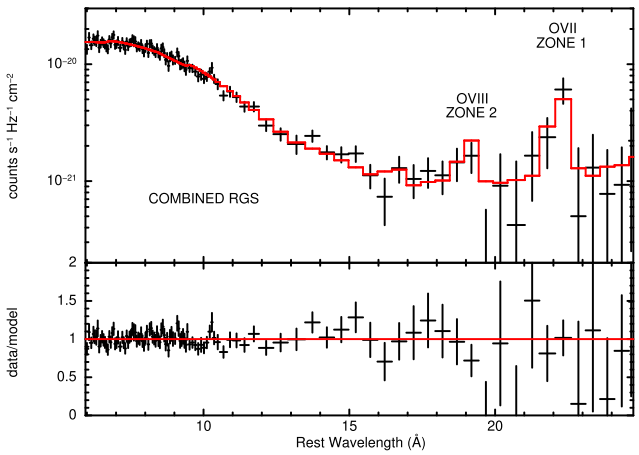


Figure 3. *Top*: combined RGS1 + RGS2 spectrum of the analysed data, rebinned here for visual purposes only. The two photoionized plasma components Zone 1 and Zone 2 model the O VII and O VIII emission components, respectively. *Bottom*: data-to-model ratio of the best-fitting model adopted for the RGS spectrum.

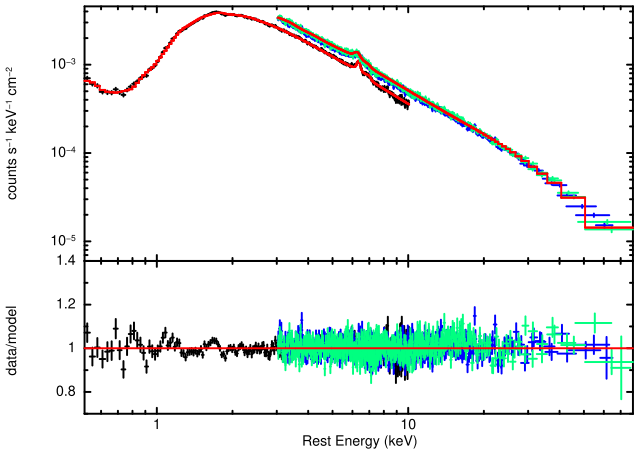


Figure 4. Broad-band *XMM–Newton* and *NuSTAR* spectra analysed here, fitted with the broad-band best-fitting model described in Section 3.3. The black spectrum is the EPIC-pn from *XMM–Newton*, while blue and green spectra are the *NuSTAR* observations of Epochs 1 and 2, respectively. As in Fig. 2, the two FPM spectra of each observation have been plotted with the same colour. *Bottom*: data-to-model ratio of EPIC-pn and FPM spectra in the 0.5–79 keV band.

3.2 Photoionized plasma in the RGS spectrum

In order to reproduce all the complexities of the broad-band data, we analyse the combined RGS spectra of the *XMM–Newton* observation.

We initially consider the unbinned RGS spectrum. Therefore, we adopt a Cash statistic for our fits (Cash 1979), as each bin has an insufficient number of counts to adopt the χ^2 statistic (e.g. Kaastra 2017). We observe the presence of two prominent emission lines at ∼19 and ∼22 Å. We then select a small spectral region of ∼100 channels around these lines and look for Gaussian lines, assuming negligible width ($\sigma = 0$). We find a Gaussian line at rest energy $E = (22.08 \pm 0.01)$ Å ($\Delta C/\Delta\mathrm{dof} = 35/2$) and a second one at $E = (18.98 \pm 0.01)$ Å ($\Delta C/\Delta\mathrm{dof} = 31/2$). As these emission lines are most likely produced by O VII and O VIII, respectively, this is a strong hint of the presence of ionized material.

We bin the spectrum with wavelength bins of $\Delta\lambda = 0.05$ Å, which samples the resolution of the RGS (e.g. den Herder et al. 2001). We still adopt a Cash statistic. We first fit the $\lambda = 6$–25 Å spectrum with the superposition of an absorbed and unabsorbed power law. The secondary power law is assumed to be a scattered component from the main one, therefore we tie the two photon indices and we let the normalizations vary independently. We find a photon index of $\Gamma = 1.6 \pm 0.3$, a column density $N_\mathrm{H} = (2.0 \pm 0.2) \times 10^{22}$ cm^{-2}. The goodness of fit is $C/\mathrm{dof} = 441/369$. Significant residuals are present at ∼19 Å, and ∼22 Å, as expected from the preliminary analysis described above. We replace the scattering power law with a CLOUDY photoionized plasma component (Ferland et al. 1998), as described in Bianchi et al. (2010). We find a ionization parameter $\log U = 1.83^{+0.07}_{-0.04}$ (corresponding to $\log \xi \sim 3.3$ erg cm s^{-1}, if we adopt an average spectral energy distribution, as described by Crenshaw & Kraemer 2012) and a column density $N_\mathrm{H} = (4.0^{+0.3}_{-0.5}) \times 10^{21}$ cm^{-2}. The statistic improves to $C/\mathrm{dof} = 420/367$, which improves the fit in the ∼19 Å region. However, residuals are still present in the ∼22 Å spectral region, which are not properly fitted by a single photoionized plasma component. Hence, we include a second photoionized plasma component, for which we obtain $\log U = -1.2 \pm 0.2$ ($\log \xi/\mathrm{erg\,cm\,s^{-1}} \sim 0.3$) and $N_\mathrm{H} = 2^{+3}_{-1} \times 10^{21}$ cm^{-2}, improving the fit to $C/\mathrm{dof} = 381/364$. As shown in Fig. 3, the addition of a second photoionized plasma component is able to account for both the 19 and 22 Å spectral regions. We name the low-ionization zone as Zone 1 and the high ionization one as Zone 2. With both the ionized plasma components, the best-fitting power-law photon index is $\Gamma = 1.9^{+0.1}_{-0.2}$ and the absorption column density is $N_\mathrm{H} = (2.2 \pm 0.1) \times 10^{22}$ cm^{-2}.

3.3 Final broad-band model

We now consider the broad-band ($E = 0.5$–79 keV) EPIC-pn and *NuSTAR* data.

We use the RGS results described in Section 3.2 to model the soft X-ray emission, therefore we add to the hard energy band model described in Section 3.1 two Galaxy-absorbed photoionized plasma components with ionization and column density values fixed to the ones obtained with the RGS fit, allowing the two normalizations to vary. The XSPEC expression of the broad band model is therefore

```
TBabs*zTBabs*(zcutoffpl+vashift
*(relxill+xillver)) +
+TBabs*(cloudy1 + cloudy2).
```

The statistic of this model is $\chi^2/\mathrm{dof} = 2579/2238$. There are some residuals in the $E < 2$ keV energy band. Given the best signal-to-noise ratio of EPIC-pn data with respect to the RGS, we free the two photoionized components, obtaining a better fit ($\chi^2/\mathrm{dof} = 2492/2234 \simeq 1.11$, corresponding to $\Delta\chi^2/\Delta\mathrm{dof} = 87/4$). The low ionization Zone 1 has an unconstrained ionization ($\log U > -2$) with a column density $N_\mathrm{H} = (5 \pm 4) \times 10^{21}$ cm^{-2}, consistent with the RGS result. The high ionization Zone 2 has a ionization parameter of $\log U = 2.2^{+0.1}_{-0.3}$, consistent with the RGS, while the column density is $N_\mathrm{H} = (6 \pm 1) \times 10^{22}$ cm^{-2}. A few residuals are still present, as shown in Fig. 4, possibly arising from emission lines at $E \simeq 0.80$, $E \simeq 1.16$, and $E \simeq 1.68$ keV. These lines are not present in the RGS spectrum, therefore their nature is not clear, but they are unlikely to arise from the source. Moreover, the most significant of these lines has a centroid energy of $E = 1.67^{+0.01}_{-0.03}$ keV, which is not a known emission line in AGNs. However, investigating the nature of these lines is beyond the scope of this paper.

We find a column density of the absorber of $N_\mathrm{H} = (1.35 \pm 0.01) \times 10^{22}$ cm^{-2}. The main power law parameters are a photon index of

Downloaded from https://academic.oup.com/mnras/article/526/3/3540/7274144 by guest on 04 December 2024

Table 3. Table of the best-fitting model values of the broad-band X-ray spectrum ($E = 0.5$–79 keV). The goodness of fit for this model is $\chi^2/\mathrm{dof} = 2492/2234$. Given the marginal detection here, the absorption feature at 7.7 keV is reported in the table but the goodness of fit refers to the model without the absorption feature.

Parameter	Epoch 1	Epoch 2
Absorption		
$N_{\rm H}$ (10^{22} cm^{-2})	1.35 ± 0.01	–
Central source		
Γ	1.85 ± 0.01	–
E_c (keV)	131^{+10}_{-9}	–
Norm$_{\rm PL}$ (10^{-2} cm^{-2} s^{-1} keV^{-1})	$2.44^{+0.03}_{-0.04}$	$2.57^{+0.04}_{-0.05}$
Distant reflection (XILLVER)		
Fe abundance	$1.4^{+0.3}_{-0.2}$	–
Inclination ($^\circ$)	$45^{\circ\,a}$	–
$\log \xi$ (erg cm s^{-1})	0^a	–
Norm$_{\rm XIL}$ (10^{-4} cm^{-2} s^{-1} keV^{-1})	$1.9^{+0.1}_{-0.2}$	$2.0^{+0.5}_{-0.4}$
Relativistic disc reflection (RELXILL)		
$R_{\rm in}$ (R_g)	$40^{+23\,b}_{-16}$	–
a	0^a	–
Log ξ	$2.9^{+0.4}_{-0.2}$	–
Inclination ($^\circ$)	$41^{+9\ b}_{-11}$	–
Norm$_{\rm REL}$ (10^{-5} cm^{-2} s^{-1} keV^{-1})	4 ± 1	2 ± 1
Photoionized emission Zone 1 (CLOUDY, EPIC-pn)		
Log U	>-2	–
$N_{\rm H}$ (cm^{-2})	$(5 \pm 4) \times 10^{21}$	–
Photoionized emission Zone 2 (CLOUDY, EPIC-pn)		
Log U	$2.2^{+0.1}_{-0.3}$	–
$N_{\rm H}$ (cm^{-2})	$(6 \pm 1) \times 10^{22}$	–
Fluxes		
$F_{0.5\text{–}2\,\rm keV}$ (10^{-12} erg s^{-1} cm^{-2})	8.19 ± 0.04	–
$F_{2\text{–}10\,\rm keV}$ (10^{-11} erg s^{-1} cm^{-2})	$7.40^{+0.02}_{-0.01}$	7.92 ± 0.02
Unabsorbed luminosity		
$L_{2\text{–}10\,\rm keV}$ (10^{43} erg s^{-1})	1.24 ± 0.01	1.30 ± 0.02

[a]Frozen parameters. [b]The internal radius $R_{\rm in}$ is obtained by freezing the inclination $\iota = 45^\circ$, while the inclination is obtained by freezing $R_{\rm in} = 45 R_g$, which would be unconstrained if both the parameters were allowed to vary. Parameters that are tied between Epochs 1 and 2 are only reported in the Epoch 1 column.

$\Gamma = 1.85 \pm 0.01$, with a cut-off energy $E_{\rm cut} = 131^{+10}_{-9}$ keV. The best-fitting values of the broad-band model are summarized in Table 3.

4 DISCUSSION

4.1 Continuum

As shown in Section 3.3, the X-ray continuum is well fitted by a photon index of $\Gamma = 1.85 \pm 0.01$ and a cut-off energy $E_{\rm cut} = 131^{+10}_{-9}$ keV. Both the photon index and the cut-off energy are consistent with previous *NuSTAR* results of this AGN (Baloković et al. 2015), where a cut-off energy of $E_{\rm cut} = 116^{+6}_{-5}$ keV was found. In Fig. 5 the $\Gamma - E_{\rm cut}$ contour plot for 1σ, 2σ, and 3σ confidence levels is shown. We also investigate the possible variability of the photon index and cut-off energy, which was suggested in past observations of MCG-5-23-16 (Zoghbi et al. 2017). If we let Γ and $E_{\rm cut}$ to vary independently between Epoch 1 and Epoch 2, keeping the two parameters tied between *XMM–Newton* and *NuSTAR* in Epoch 1, we obtain identical photon indices. In Epoch 1, the cut-off energy is $E_{\rm cut,1} = 113^{+12}_{-10}$ keV,

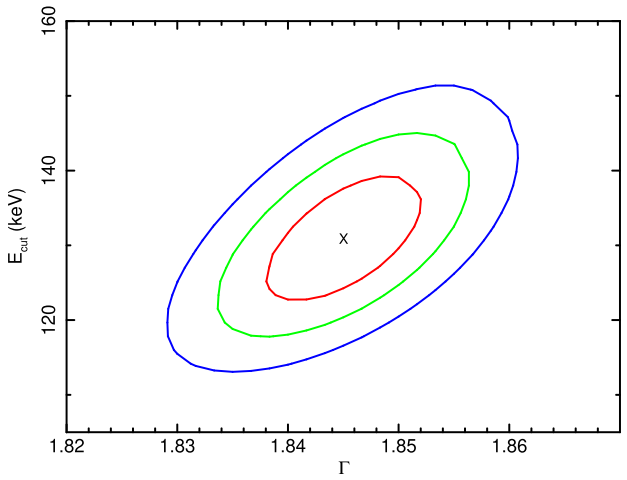


Figure 5. Contour plot $E_{\rm cut} - \Gamma$ for the broad-band model. The red, green, and blue lines represents the 68 per cent (1σ), 95 per cent (2σ), and 99.7 per cent (3σ) confidence levels, while the best-fitting value is marked by an X.

while for Epoch 2 the cut-off energy is $E_{\rm cut,2} = 140^{+18}_{-16}$ keV, which are consistent at the 90 per cent confidence value.

The photon index and the cut-off energy are tightly related to the coronal electron temperature and optical depth (e.g. Petrucci et al. 2001; Middei et al. 2019), which could be investigated with Comptonization models. We estimate the temperature kT and the optical depth τ of the corona of MCG-5-23-16 by replacing the cut-off power law continuum with the physical model COMPPS (Poutanen & Svensson 1996) assuming a slab geometry (i.e. we set the parameter `geom` to 1). We assume a blackbody temperature of the seed photons of 10 eV and we find $kT = 26 \pm 1$ keV and $\tau = 1.25 \pm 0.05$, consistent at the 90 per cent confidence level with Baloković et al. (2015) and Marinucci et al. (2022). If we explore a spherical geometry (i.e. `geom` $= 0$) we obtain $kT = 28^{+6}_{-5}$ keV and $\tau = 4.7^{+0.5}_{-1.9}$.

4.2 Reflection

The reflection spectrum of MCG-5-23-16 is comprised of two different components. The distant reflecting medium, also responsible for the narrow core of the Fe Kα emission line, is likely associated with the obscuring torus. The inner reflecting region, producing the broad component of the emission line, is instead likely associated with the accretion disc.

The iron abundance is kept tied between the two reflectors and it is $A_{\rm Fe} = 1.4^{+0.3}_{-0.2}$. We initially keep the inclination fixed at 45°, and we assume a non-spinning black hole, i.e. $a = 0$. We note that if we assume a different value of the black hole spin, such as a maximally spinning black hole with $a = 0.998$, our best-fitting values are left almost unchanged at the 90 per cent confidence level. We also assume an radial emissivity index of -3. The disc turns out to be truncated, with an inner radius of $R_{\rm in} = 40^{+23}_{-16}\,R_g$, in agreement with the past observations of this AGN. The ionization parameter of the disc reflector is $\log \xi/(\mathrm{erg\,cm\,s^{-1}}) = 2.9^{+0.4}_{-0.2}$, while that of the distant reflector is consistent with a neutral or weakly ionized medium. If we fix the inner radius to 45 R_g and let the inclination free we obtain $\iota = 41^{\circ\ +9}_{\ -11}$. However, the two parameters are strongly degenerate, and if we allow them both to vary we do not constrain the inner radius, obtaining $R_{\rm in} > 6\ R_g$ with an inclination of $\iota = 31 \pm 10^\circ$.

Downloaded from https://academic.oup.com/mnras/article/526/3/3540/7274144 by guest on 04 December 2024

Although this inclination value is consistent with the one obtained assuming a truncated disc, extremely low inclinations are highly unlikely given the persistent moderate obscuration, which is always observed in MCG-5-23-16. Indeed, a persistent obscuration with values of the column density of a few 10^{22} cm^{-2}, as in the case of MCG-5-23-16, is likely due to the line of sight crossing near the edge of the torus. Assuming that the torus and the accretion disc are aligned, it is unlikely that small face-on inclinations are able to describe the observed lack of absorption variability. Alternatively, the column density may be due to a galactic dust lane, but a more face-on inclination may still appear less likely given its type 1.9 optical classification (e.g. Véron et al. 1980).

We also test if a maximally spinning black hole, i.e. $a = 0.998$, changes any result when both the inner radius and inclination are let free. We find the same result, i.e. an unconstrained inner radius and a smaller inclination, with the lower value of the inner radius set to $R_{\rm in} > 1.7\ R_g$.

4.3 A possible absorption complex in the Fe K band

Some absorption residuals may be also present in the EPIC-pn data at the Fe K band. We test the possible presence of absorption lines at ∼7–10 keV with Gaussians. The inclusion of a line at ∼7.7 keV improves the fit by $\Delta\chi^2/\Delta{\rm dof} = 15/3$. If we simulate 1000 EPIC-pn spectra adopting the best-fitting model, without any absorption line, we find 55 spectra for which a spurious absorption line in the 7–9 keV is found with $\Delta\chi^2/\Delta{\rm dof} \geq 15/3$ (see e.g. Markowitz, Reeves & Braito 2006, for details on this procedure), which implies a $\lesssim 95$ per cent confidence level. While this is a marginal detection, an absorption complex was already found by Braito et al. (2007), who interpreted a feature at ∼7.7 keV as an absorption line from Fe XXVI, outflowing with velocity $v \sim 0.09c$. Therefore, purely in order to compare with the previous detection of the line, we report here its best-fit parameters.

We fit the absorption trough at ∼7.7 keV with a simple Gaussian line, with width σ left free to vary. We find an unconstrained width and therefore we fix $\sigma = 0$. We let the normalisations in Epochs 1 and 2 free to vary independently. We find a centroid energy of $E = 7.74^{+0.05}_{-0.06}$ keV, with an equivalent width of ${\rm EW}_1 = 19 \pm 5$ eV in Epoch 1 and ${\rm EW}_2 < 5$ eV in Epoch 2. Therefore, if a line is indeed present, it would be two times weaker than previously observed in Braito et al. (2007), where an equivalent width of EW ∼ 50 eV was found. This would be most likely due to a change in column density of the wind. However, the centroid energy is consistent with the one recovered in the past, which would imply an outflowing velocity of $v/c = 0.10 \pm 0.01$, if interpreted as outflowing Fe XXVI. However, we stress that the line is not indeed detected, and only mentioned here to compare it with previous 2005 observations of this AGN.

5 SUMMARY AND CONCLUSIONS

We have presented the analysis of one *XMM–Newton* and two *NuSTAR* observations of MCG-5-23-16, one of which contemporaneous with *XMM*. This is the first contemporaneous broadband observation of this AGN with the two telescopes. Both *NuSTAR* epochs are also contemporaneous with *IXPE* observations, for which upper limits on the polarization degree were observed (Marinucci et al. 2022; Tagliacozzo et al. 2023). We summarise our results in the following:

(i) We find a well constrained value of the cut-off energy at $E_{\rm cut} = 131^{+10}_{-9}$ keV. This value is consistent with previous results of *NuSTAR* analyses on this AGN and it represents an average value of the cut-off energies typically found in AGN (e.g. Tortosa et al. 2018; Kamraj et al. 2022). No variability of the cut-off energy is detected between Epochs 1 and Epoch 2. Assuming a slab (spherical) geometry of the corona, we find a coronal temperature of $kT = 26 \pm 1$ keV ($kT = 28^{+6}_{-4}$) and an optical depth $\tau = 1.25 \pm 0.05$ ($\tau = 4.7^{+0.5}_{-0.9}$), largely in agreement with previous results on this AGN.

(ii) The spectrum shows evidence of the presence of a broad line, produced by the reflection of the primary component on a truncated accretion disc, with an inner radius of $R_{\rm in} = 40^{+23}_{-16}\ R_g$.

(iii) The inclination is $\iota = 41^{\circ\,+9}_{-10}$, which is consistent with a persistent moderate obscuration as that observed for MCG-5-23-16. Indeed, we find $N_{\rm H} \sim 1.3 \times 10^{22}$ cm^{-2}, roughly constant in time-scales of decades. A persistent obscuration with such column density, if due to the absorption by the torus, would imply that the absorption occurs at the edge of the torus itself, and an inclination of ∼45°, consistent with our result, would be required. Tagliacozzo et al. (2023) showed that, even though the polarisation degree is not constrained at the 99 per cent confidence level, if we assume the inclination obtained in the present paper a wedge corona (e.g. Poutanen et al. 2018) is favoured, as in the case of NGC 4151 (Gianolli et al. 2023).

(iv) The RGS spectrum highlights the presence of two photoionized plasma components. When the EPIC-pn is fitted, the first component, denoted as Zone 1, is characterized by a ionization parameter $\log U > -2$ and a column density of $N_{\rm H} \sim 5 \times 10^{21}$ cm^{-2}, which is responsible of the O VII emission in the RGS spectrum. A second component, Zone 2, is characterized by a larger ionization parameter ($\log U \sim 2.2$) and column density of $N_{\rm H} \sim 6 \times 10^{22}$ cm^{-2}, which is instead responsible for the more ionized O VIII emission line.

(v) We also report on the marginal detection of a possible absorption line with centroid energy $E \sim 7.74$ keV. If confirmed, the line could be interpreted as blue-shifted outflowing Fe XXVI, which would imply a wind velocity of $v/c \sim 0.1c$. However, we must stress that the line is only marginally detected, due to a smaller column density with respect to the previous detection of the line (Braito et al. 2007), and we only report the possible absorption feature to compare it with its prior detection with *XMM–Newton*.

(vi) Overall, the X-ray spectrum of MCG-5-23-16 appears to be remarkably stable over the years. In fact, only moderate variations in flux and column density are observed, while the properties of the disc, such as the inner radius inferred from the broad iron line, do not appear to significantly change compared to past observations with *Suzaku* (Reeves et al. 2007), *XMM–Newton* (Braito et al. 2007), and *NuSTAR* (Baloković et al. 2015; Zoghbi et al. 2017). Furthermore, the X-ray coronal properties also appear consistent, as compared between the observations presented here and the past *NuSTAR* pointings.

Future high-resolution observations of MCG-5-23-16 with the microcalorimeter Resolve on board the upcoming X-ray mission *XRISM* (XRISM Science Team 2020) will allow us to observe the X-ray sources with unprecedented spectral resolution. XRISM observations will be able to resolve the various components of the iron line profile, such as the possible presence of ionized iron lines. Indeed, this will be groundbreaking in determining the disc parameters from the broad iron line with much larger accuracy, in particular the inner radius $R_{\rm in}$ and the inclination of the accretion disc, as the width of the narrow core and possibly any contribution from the broad-line region will be measured with unprecedented accuracy, clearly separating it from the disc-reflection component.

Downloaded from https://academic.oup.com/mnras/article/526/3/3540/7274144 by guest on 04 December 2024

Additionally, the future enhanced X-ray, timing and polarimetry mission (*eXTP*; De Rosa et al. 2019; Zhang et al. 2019), will be able to perform simultaneous spectral-timing polarimetry measurements, allowing us to put strong constraints on the emission and reflection properties of accreting SMBHs.

ACKNOWLEDGEMENTS

The authors thank the referee for significantly improving the quality of this paper with useful comments and suggestions. RS and ADR acknowledge financial support from the agreements ASI-INAF eXTP Fase B – 2020-3-HH.1-2021 and ASI-INAF no. 2017-14-H.O. JR and VB acknowledge financial support through NASA grants 80NSSC22K0474, 80NSSC22K0003, and 80NSSC22K0220. POP aknowledges financial support from the High Energy programme (PNHE) of the Scientific Research National Center (CNRS) and the French Space Agency (CNES). SB acknowledges support from PRIN MUR 2017 'Black hole winds and the baryon life cycle of galaxies: the stone-guest at the galaxy evolution supper', and from the European Union Horizon 2020 Research and Innovation Framework Programme under grant agreement AHEAD2020 n. 871158. This research has made use of data and software provided by the High Energy Astrophysics Science Archive Research Center (HEASARC), which is a service of the Astrophysics Science Division at NASA/GSFC and the High Energy Astrophysics Division of the Smithsonian Astrophysical Observatory. This research has made use of the *NuSTAR* Data Analysis Software (NUSTARDAS), jointly developed by the ASI Space Science Data Center (SSDC, Italy) and the California Institute of Technology (Caltech, USA). The research is partly based on observations obtained with *XMM–Newton*, an ESA science mission with instruments and contributions directly funded by ESA Member States and NASA.

DATA AVAILABILITY

The *XMM–Newton* data underlying this article are publicly available from the *XMM–Newton* science archive (http://nxsa.esac.esa.int/). The *NuSTAR* data are publicly available on the online archive (https://heasarc.gsfc.nasa.gov/docs/nustar/nustar_archive.html).

REFERENCES

Arnaud K. A., 1996, in Jacoby G. H., Barnes J., eds, ASP Conf. Ser. Vol. 101, Astronomical Data Analysis Software and Systems V. Astron. Soc. Pac., San Francisco, p. 17
Balestra I., Bianchi S., Matt G., 2004, A&A, 415, 437
Ballet J., 1999, A&AS, 135, 371
Baloković M. et al., 2015, ApJ, 800, 62
Baloković M. et al., 2020, ApJ, 905, 41
Bianchi S., Chiaberge M., Evans D. A., Guainazzi M., Baldi R. D., Matt G., Piconcelli E., 2010, MNRAS, 405, 553
Braito V. et al., 2007, ApJ, 670, 978
Cash W., 1979, ApJ, 228, 939
Crenshaw D. M., Kraemer S. B., 2012, ApJ, 753, 75
Dadina M., 2007, A&A, 461, 1209
Dauser T., Wilms J., Reynolds C. S., Brenneman L. W., 2010, MNRAS, 409, 1534
Dauser T., Garcia J., Parker M. L., Fabian A. C., Wilms J., 2014, MNRAS, 444, L100
De Luca A., Molendi S., 2004, A&A, 419, 837
De Rosa A. et al., 2012, MNRAS, 420, 2087
De Rosa A. et al., 2019, Sci. China Phys. Mech. Astron., 62, 29504
den Herder J. W. et al., 2001, A&A, 365, L7
Dewangan G. C., Griffiths R. E., Schurch N. J., 2003, ApJ, 592, 52
Fabian A. C., Lohfink A., Kara E., Parker M. L., Vasudevan R., Reynolds C. S., 2015, MNRAS, 451, 4375
Fabian A. C., Lohfink A., Belmont R., Malzac J., Coppi P., 2017, MNRAS, 467, 2566
Ferland G. J., Korista K. T., Verner D. A., Ferguson J. W., Kingdon J. B., Verner E. M., 1998, PASP, 110, 761
Frontera F., Amati L., Zdziarski A. A., Belloni T., Del Sordo S., Masetti N., Orlandini M., Palazzi E., 2003, ApJ, 592, 1110
García J., Kallman T. R., 2010, ApJ, 718, 695
García J., Dauser T., Reynolds C. S., Kallman T. R., McClintock J. E., Wilms J., Eikmann W., 2013, ApJ, 768, 146
García J. et al., 2014, ApJ, 782, 76
Gianolli V. E. et al., 2023, MNRAS, 523, 4468
HI4PI Collaboration, 2016, A&A, 594, A116
Haardt F., Maraschi L., 1991, ApJ, 380, L51
Haardt F., Maraschi L., 1993, ApJ, 413, 507
Ingram A. et al., 2023, MNRAS, 525, 5437
Kaastra J. S., 2017, A&A, 605, A51
Kamraj N. et al., 2022, ApJ, 927, 42
Lightman A. P., Zdziarski A. A., 1987, ApJ, 319, 643
Magdziarz P., Zdziarski A. A., 1995, MNRAS, 273, 837
Marinucci A. et al., 2014, ApJ, 787, 83
Marinucci A. et al., 2022, MNRAS, 516, 5907
Markowitz A., Reeves J. N., Braito V., 2006, ApJ, 646, 783
Matzeu G. A. et al., 2023, A&A, 670, A182
Middei R., Bianchi S., Marinucci A., Matt G., Petrucci P. O., Tamborra F., Tortosa A., 2019, A&A, 630, A131
Middei R. et al., 2021, A&A, 647, A102
Miniutti G., Fabian A. C., 2004, MNRAS, 349, 1435
Palmeri P., Mendoza C., Kallman T. R., Bautista M. A., Meléndez M., 2003, A&A, 410, 359
Petrucci P. O. et al., 2001, ApJ, 556, 716
Pounds K. A., Reeves J. N., King A. R., Page K. L., O'Brien P. T., Turner M. J. L., 2003, MNRAS, 345, 705
Poutanen J., Svensson R., 1996, ApJ, 470, 249
Poutanen J., Veledina A., Zdziarski A. A., 2018, A&A, 614, A79
Reeves J. N. et al., 2007, PASJ, 59, 301
Ricci C. et al., 2017, ApJS, 233, 17
Serafinelli R., Tombesi F., Vagnetti F., Piconcelli E., Gaspari M., Saturni F. G., 2019, A&A, 627, A121
Serafinelli R., Braito V., Reeves J. N., Severgnini P., De Rosa A., Della Ceca R., Turner T. J., 2023, A&A, 672, A10
Shapiro S. L., Lightman A. P., Eardley D. M., 1976, ApJ, 204, 187
Sunyaev R. A., Titarchuk L. G., 1980, A&A, 86, 121
Tagliacozzo D. et al., 2023, MNRAS, 525, 4735
Tombesi F., Cappi M., Reeves J. N., Palumbo G. G. C., Yaqoob T., Braito V., Dadina M., 2010, A&A, 521, A57
Tortosa A., Bianchi S., Marinucci A., Matt G., Petrucci P. O., 2018, A&A, 614, A37
Ursini F., Matt G., Bianchi S., Marinucci A., Dovčiak M., Zhang W., 2022, MNRAS, 510, 3674
Véron P., Adam G., Lindblad P. O., Veron M. P., Zuiderwijk E. J., 1980, A&A, 87, 245
Weaver K. A., Yaqoob T., Mushotzky R. F., Nousek J., Hayashi I., Koyama K., 1997, ApJ, 474, 675
Wilkins D. R., Fabian A. C., 2012, MNRAS, 424, 1284
Science XRISM, 2020, preprint (arXiv:2003.04962)
Zhang S. et al., 2019, Sci. China Phys. Mech. Astron., 62, 29502
Zoghbi A. et al., 2017, ApJ, 836, 2

This paper has been typeset from a TEX/LATEX file prepared by the author.

© 2023 The Author(s)
Published by Oxford University Press on behalf of Royal Astronomical Society

Downloaded from https://academic.oup.com/mnras/article/526/3/3540/7274144 by guest on 04 December 2024